

Interface-assisted in-situ growth of halide electrolytes eliminating interfacial challenges of all-inorganic solid-state batteries

Changhong Wang^{a,1}, Jianwen Liang^{a,1}, Ming Jiang^b, Xiaona Li^a, Sankha Mukherjee^b, Keegan Adair^a, Matthew Zheng^a, Yang Zhao^a, Feipeng Zhao^a, Shuming Zhang^a, Ruying Li^a, Huan Huang^c, Shangqian Zhao^d, Li Zhang^d, Shigang Lu^d, Chandra Veer Singh^{b,**}, Xueliang Sun^{a,*}

^a Department of Mechanical and Materials Engineering, University of Western Ontario, 1151 Richmond St, London, Ontario, N6A 3K7, Canada

^b Department of Materials Science and Engineering, University of Toronto, Toronto, Ontario, M5S 3E4, Canada

^c Glabat Solid-State Battery Inc., 700 Collip Circle, London, Ontario, N6G 4X8, Canada

^d China Automotive Battery Research Institute Co., Ltd., 5th Floor, No. 43, Mining Building, North Sanhuan Middle Road, Haidian District, Beijing, P.C. 100088, China

ARTICLE INFO

Keywords:

Interface-assisted in-situ growth
Halide electrolyte Li_3InCl_6
Interfacial challenges
All-inorganic solid-state batteries

ABSTRACT

All-inorganic solid-state batteries (AIBBs) have received considerable attention due to their excellent safety and high energy density. However, large interfacial challenges between oxide cathodes and inorganic solid electrolytes dramatically hinder AIBB development. Here we successfully eliminate the long-standing interfacial challenges by in-situ interfacial growth of a highly Li^+ -conductive halide electrolyte (Li_3InCl_6 , LIC) on the cathode surface. Owing to strong interfacial interaction, high interfacial ionic conductivity ($>1 \text{ mS cm}^{-1}$), and excellent interfacial compatibility, LiCoO_2 with 15 wt% LIC exhibits a high initial capacity of 131.7 mAh.g^{-1} at 0.1C ($1\text{C} = 1.3 \text{ mA cm}^{-2}$) and can be operated up to 4C at room temperature. The discharge capacity retains 90.3 mAh.g^{-1} after 200 cycles. Moreover, a high areal capacity of 6 mAh cm^{-2} is demonstrated with a high loading of 48.7 mg cm^{-2} . This work offers a versatile approach to eliminate interfacial challenges of AIBBs toward high-energy density and high-power density.

1. Introduction

All-inorganic solid-state batteries (AIBBs) have received considerable attention in recent years because of their significant improvements in safety and energy density over liquid cells [1–3]. However, several main challenges impede the development of AIBBs, including (1) insufficient ionic conductivity of inorganic solid-state electrolytes (ISEs) [4]; (2) large interfacial resistance between electrode materials and SEs, which originates from poor solid-solid contact and detrimental interfacial reactions [5,6]; (3) lithium dendrite growth in ISEs [7]. With the continuous efforts over the past years, various ISEs have been developed with high ionic conductivity, such as sulfide electrolytes ($\text{Li}_{10}\text{GeP}_2\text{S}_{12}$ [4], 12 mS cm^{-2} , $\text{Li}_{9.54}\text{Si}_{1.74}\text{P}_{1.44}\text{S}_{11.7}\text{Cl}_{0.3}$ [8], 25 mS cm^{-2}), their ionic conductivity even surpasses those of conventional liquid electrolytes and gel polymers [9]. To suppress the lithium dendrite growth in ISEs,

various effective strategies have also been proposed, such as interface modification and chemical composition tuning of ISEs [10–15].

In contrast to the tremendous success in developing highly lithium-ion (Li^+)-conductive ISEs and suppressing lithium dendrite growth in ISEs, the interfacial challenges between oxide cathodes and ISEs have not been successfully addressed yet [16]. Until now, sulfide-based AIBBs still suffer from detrimental interfacial reactions and poor solid-solid contact between sulfide electrolytes and oxide cathodes. To suppress the interfacial reactions, interfacial coating such as LiNbO_3 , LiTaO_3 , and $\text{Li}_4\text{Ti}_5\text{O}_{12}$ is indispensable [17–19]. However, the low ionic conductivity (10^{-6} – $10^{-9} \text{ S cm}^{-1}$) of these interfacial coating materials, which is several orders of magnitude lower than those of inorganic solid electrolytes themselves (including sulfide electrolytes and oxide electrolytes), significantly restricts the electrochemical performance of AIBBs [20]. Besides, the uniformity of the interfacial coating layer on

* Corresponding author.

** Corresponding author.

E-mail addresses: chandrasekar.singh@utoronto.ca (C.V. Singh), xsun9@uwo.ca (X. Sun).

¹ These authors contributed equally to this work.

the cathode particle surface is hard to control. Consequently, interfacial reactions would not be fully suppressed. To improve the solid-solid contact, 30% ISE is normally added into the cathode composites by mechanical mixing to achieve ample solid-solid contact between oxide cathodes and ISEs. The large amount of ISEs in the cathode composite dilutes the energy density of AIBSBs [21–23]. Based on the pouch cell evaluation, the mass ratio of ISE in cathode composites should be no more than 15% to achieve a high energy density of 300–500 Wh kg⁻¹ [22,23]. In recent years, the liquid-phase method has been developed to achieve sufficient solid-solid contact with a small amount of ISEs [24, 25]. However, the solvent-involved process generally decreases the ionic conductivity of ISEs, consequently depressing the electrochemical performance of AIBSBs [26,27]. All things considered, so far there is no versatile strategy that can simultaneously achieve both high interfacial ionic conductivity (>1 mS cm⁻¹) and intimate solid-solid contact with a small amount of ISEs (<15%).

Inspired by the high ionic conductivity of halide electrolytes (Li₃MX₆, M = Y, In et al., X = Cl, Br) and their excellent stability against high-voltage cathodes [28–31], here we report an in-situ interfacial growth of halide electrolytes (Li₃InCl₆, LIC) on electrode materials (LiCoO₂, LCO) from aqueous solution for the first time. As little as 15 wt % LIC was uniformly distributed in the cathode composite, which constructs a three-dimensional (3D) continuous Li⁺ conduction pathway and guarantees the high energy density of AIBSBs. Moreover, the high ionic conductivity (1.5 mS cm⁻¹) and high-voltage stability of LIC, as well as intimate solid-solid contact, ensure the ultra-small interfacial resistance between LCO and LIC (5.3 Ω cm²). As a result, the LIC@LCO-15 wt% electrode exhibits a high initial discharge capacity of 131.7 mAh.g⁻¹ with an initial Coulombic efficiency of 92.7% at 0.1C. The gravimetric energy density of AIBSBs is up to 512 Wh.kg⁻¹ (electrode-based). Even at a high rate of 4C (5.2 mA cm⁻²), 28.5 mAh.g⁻¹ can be obtained, which corresponds to 1300W kg⁻¹. Furthermore, a high areal capacity of 6.0 mAh.cm⁻² can be realized with a high LCO loading of 48.7 mg cm⁻². This work provides a versatile approach to eliminate

the interfacial challenges between oxide cathodes and ISEs toward high-energy-density and high-power-density AIBSBs.

2. Results and discussion

Synthesis and Characterization of LIC and LIC@LCO: In-situ interfacial growth of LIC on LCO is schematically shown in Fig. 1a. InCl₃ and LiCl with a stoichiometric ratio of 1:3 were dissolved in deionized water, forming a transparent Li₃InCl₆.nH₂O solution. Subsequently, LiCoO₂ was added into the transparent solution. After evaporation of water solution under 100 °C, the obtained dry powder was transferred to a vacuum oven and heated at 200 °C for 5 h to dehydrate. Then yielded Li₃InCl₆-coated LiCoO₂ (LIC@LCO) cathode composites were used for AIBSBs directly. Detailed synthesis procedures can be found in Supplementary Information. It should be noted that the thickness of the LIC layer can be adjusted by controlling the LIC-to-LCO ratio. In general, the less ISE content in the electrode composite, the higher the energy density of solid-state batteries [23]. However, too little ISEs in electrode composites limits the ionic contact between electrode materials and ISEs. Therefore, the best ratio between LIC and LCO requires optimization. As shown in Fig. S1, LCO surface is not fully covered with 5 wt% LIC but can be completely coated with 10 wt% LIC. With 15 wt% LIC (Fig. 1b–c), not only is the surface covered but also the gap between LCO particles is filled, thus constructing 3D continuous Li⁺-conduction pathways in the cathode composites (labeled as LIC@LCO-15 wt%) (Fig. S1i). Fig. 1b–d presents an SEM image of LIC@LCO-15 wt% and its corresponding energy-dispersive X-ray spectroscopy (EDX) elemental mapping of O and Cl, respectively, confirming the uniform distribution of LCO in the LIC matrix. To reveal the solid-solid contact beneath the surface, a cross-section of LIC@LCO-15 wt% was fabricated by focused ion beam (FIB) and the corresponding EDS mappings of Co, O, In, Cl are displayed in Fig. 1e–g, respectively, showing that LCO is surrounded by LIC with 3D continuous Li⁺ percolation networks. Furthermore, X-ray diffraction (XRD) was also

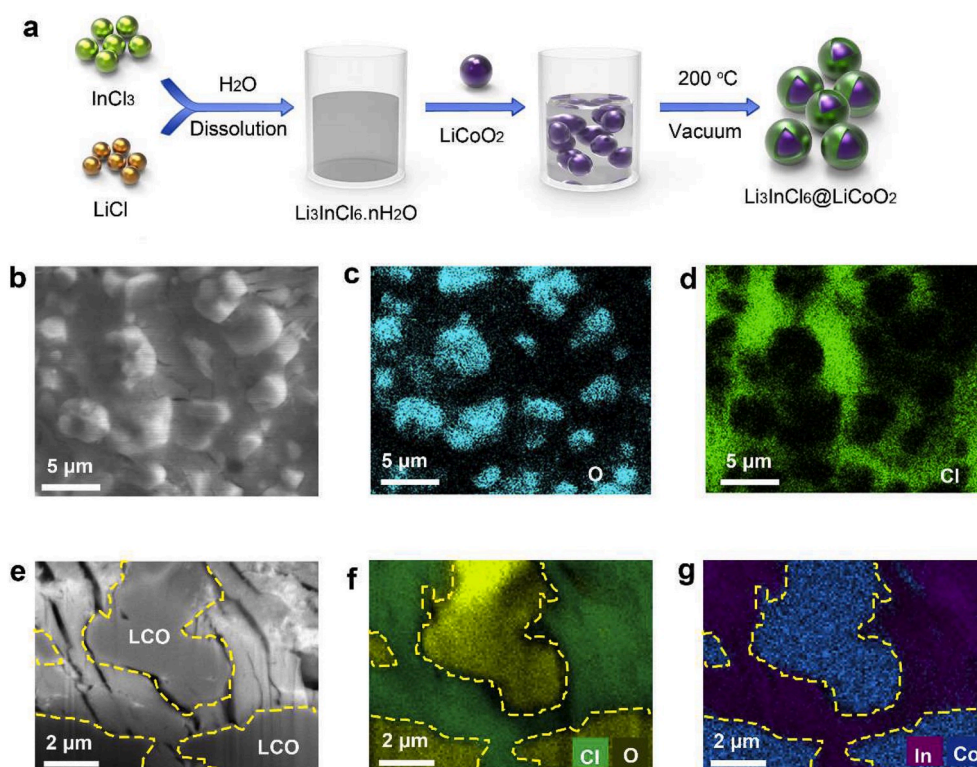


Fig. 1. (a) Illustration of the in-situ synthesis of Li₃InCl₆ on LiCoO₂ (LIC@LCO). (b) SEM image of LIC@LCO-15 wt%. (c) Elemental O mapping. (d) Elemental Cl mapping. (e) Cross-sectional SEM image of LIC@LCO-15 wt%. (f) Elemental Cl and O combined mapping. (g) Elemental In and Co combined mapping.

conducted to determine the crystallinity of the LIC layer. As displayed in Fig. S2, all the LIC@LCO electrodes exhibit strong XRD patterns associated with LCO. A small peak (131) at 34.3° originating from the LIC is identified in LIC@LCO-15 wt% and LIC@LCO-10 wt% while 5% LIC@LCO does not show the (131) peak due to the lower amount of LIC on the LCO surface, suggesting that the crystalline LIC is successfully coated on LCO. Considering that copper X-ray radiation yields a strong fluorescence background of LCO, which may hide some information of LIC@LCO composites, particularly decomposed phases and/or impurities of LIC. To double confirm the successful synthesis and interfacial compatibility of LIC on the LCO surface, LIC@LCO composites were further analyzed by micro-XRD using cobalt radiation (Fig. S3), in which only LCO and LIC phases were identified, further confirming that LIC is successfully grown on the LCO surface.

Electrochemical impedance spectroscopy (EIS) analysis in Figs. S4a–4b reveals the high ionic conductivity of LIC (1.5 mS cm^{-1}) at 25°C and the small activation energy of 0.35 eV , which is comparable (or surpassing) to that of current-mainstream oxide and sulfide electrolytes [16]. LIC precipitated from water is consisted of lots of small particles, as displayed in Figs. S4c–4d. The primary particle size of LIC is approximately $300\text{--}500 \text{ nm}$. Fig. S5 shows the slow-scanned XRD pattern and Rietveld refinement results, showing that LIC has a monoclinic unit cell (C2/m (12), ICSD No.04-009-9027) with the cell parameters of $a = 6.403395 \text{ \AA}$, $b = 11.065896 \text{ \AA}$, $c = 6.379085 \text{ \AA}$, $\alpha = \gamma = 90.0000^\circ$, $\beta = 109.8138^\circ$. The detailed structural parameters are tabulated in Table S1. The high ionic conductivity and low activation energy of LIC is due to high Li^+ vacancy content (33.3%) in its distorted monoclinic rock-salt structure [31–33].

Interfacial Interaction between LIC and LCO: It should be mentioned that the LIC on the LCO surface is not particle-like but a continuous film, implying that the nucleation process of LIC in water is different from the LCO surface. The underlying reason is possibly related to the interfacial interaction between LCO and LIC. X-ray photoelectron spectroscopy (XPS) was performed to analyze the interface interaction. In $3d_{5/2}$ and $3d_{3/2}$ peaks are located at 446.2 eV and 453.8 eV , respectively, which corresponds to the In^{3+} bonding state of LIC (Fig. 2a) [30,34]. There is no energy shift found in the $\text{In } 3d$ spectra between

LIC@LCO and pure LIC, suggesting that the chemical states of In on LIC@LCO surface are the same as that in pristine LIC. This result also indicates the successful synthesis of LIC on the LCO surface. For the $\text{O } 1s$ spectra (Fig. 2b), the green peak at 529.7 eV is characteristic of O atoms in the LCO crystal lattice [35], while the orange peak at a relatively higher binding energy of 531.7 eV is associated with oxygen-containing species or dangling oxygen bonds at the LCO surface [35]. Interestingly, the intensity of the orange peaks increases from 60% to 77% in LIC@LCO, suggesting that more oxygen-rich species are formed at the LIC/LCO interface, which may be originated from the interaction between Cl and O. In $\text{Cl } 2p$ spectra (Fig. 2c), pure LIC only shows a pair of red peaks ($\text{Cl } 2p_{3/2}$ and $\text{Cl } 2p_{1/2}$) at 199.6 eV and 201.2 eV , respectively, which are associated with In–Cl and/or Li–Cl bonds in LIC. However, a pair of blue peaks at higher binding energy (200.6 eV and 202.2 eV) are found after coating LIC on LCO, implying that Cl of LIC is involved in the interfacial interaction between LIC and LCO. Based on the $\text{O } 1s$ and $\text{Cl } 2p$ spectra, we presumed that the O of LCO interacts with the Cl of LIC at the LIC@LCO interface. This interfacial interaction assists the uniform nucleation process of LIC on the LCO surface. Therefore, LIC tends to conformably grow on the LCO surface. Resultantly, the LIC on the LCO surface is a continuous film, not particles. To further confirm the interfacial interaction LIC and LCO with the same mass ratio (15%:85%) were mechanically mixed and further analyzed by XPS (Fig. S6), no such interfacial reaction was identified, further confirming the interfacial interaction is originated from the in-situ interfacial synthesis. Therefore, the in-situ interfacial growth of LIC on the LCO surface is a unique interface-assisted process, which is completely different from the dissolution-precipitation process that previously demonstrated in sulfide-based AIBSs [24,26,36].

To verify the interfacial interaction, a density functional theory (DFT) calculation was performed. The schematic views of LCO and LIC are shown in Fig. S7 and their lattice parameters are summarized in Table S2. Furthermore, the lattice parameters and surface energies of LCO(110), LIC(100), LIC(010), LIC(001), LIC(110) and LIC(111) are calculated and listed in Table S3. The experimental measurements and previous DFT simulations indicate the existence of energetically favored (110)-oriented LCO surface [37–39]. Furthermore, (110) surfaces in

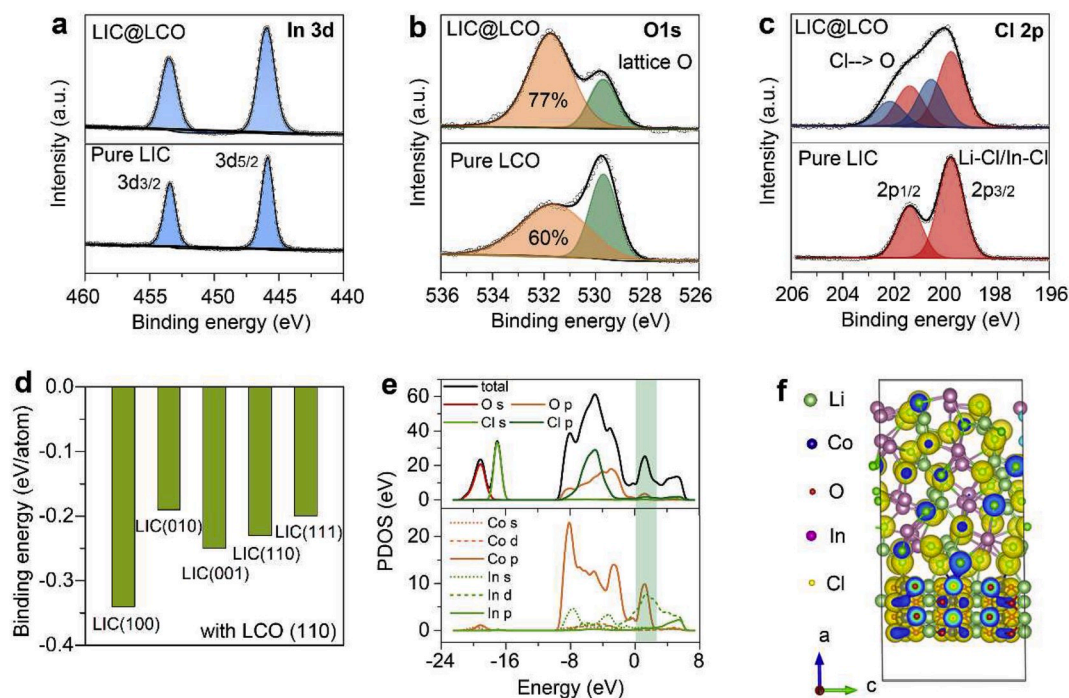


Fig. 2. Chemical Interaction between LIC and LCO. XPS spectra of LIC@LCO-15 wt%. (a) In 3d spectra. (b) O 1s spectra. (c) Cl 2p spectra. (d) The binding energy between the LCO (110) and different LIC surfaces. (e) PDOS of s, p, d orbitals of O, Cl, In, and Co. (f) Differential charge density of the LCO(110)/LIC(100) interface.

LCO particles provide Li^+ conduction paths along with the (110) direction [38,39]. Therefore, we selected (110) face as a representative surface of LCO, and the surface energy of LCO(110) was calculated to be 10.60 eV nm^{-2} . Fig. 2d displays the binding energies between the LCO (110) and different LIC faces, which indicates that LCO has high binding energy with LIC, and the strongest binding energy of -0.34 eV/atom is found between the LCO(110) and LIC(100) (Table S4). Fig. 2e shows the partial density of state (PDOS) of Co, In, Cl, and O, respectively. The absence of an energy gap at the Fermi level indicates the good electronic conductivity of LIC@LCO composites. Also, the p orbital overlap of Cl and O indicates the interaction between Cl and O, as highlighted by the green shadow region. Furthermore, the differential charge density of the LCO(110)/LIC(100) interface clearly showed the charge overlap of Cl and O at the interface (Fig. 2f), indicative of the coordination between Cl and O at the LCO/LIC interface. The strong interfacial interaction also assisted the nucleation process of LIC on the LCO surface. That is why the LIC on the LCO surface is a continuous film, not particle-like.

Electrochemical Performance of LIC@LCO in AIBSBs: LIC@LCO-based AIBSBs were evaluated at 0.1C ($1\text{C} = 1.3 \text{ mA cm}^{-2}$) at room temperature due to high ionic conductivity of LIC (1.5 mS cm^{-1}). The initial charge and discharge curves are presented in Fig. 3a. With the increase of the LIC-to-LCO ratio, the polarization between charge and discharge curves is suppressed and the discharge capacity is significantly increased. With 15 wt% LIC, the initial charge capacity is 142.1 mAh g^{-1} and the initial discharge capacity is 131.7 mAh g^{-1} with an initial

Coulombic efficiency of 92.7%. The corresponding energy density is up to 513 Wh kg^{-1} . If mechanically mixing 15% LIC with 85% LCO, the initial discharge capacity is only 68.1 mAh g^{-1} because of the insufficient solid-solid contact between LCO and LIC (Fig. S8). It should be highlighted that the charge/discharge curves of LIC@LCO-15 wt% are overlapping with those of LCO in liquid electrolytes at the same current density of 0.13 mA cm^{-2} (Fig. S9), which implies the full utilization of LCO in AIBSB with ultrafast interfacial Li^+ conduction as fast as that in liquid cells. With 10 wt% and 5 wt% LIC, LCO discharges at 90.9 mAh g^{-1} and 39.9 mAh g^{-1} , respectively, which is caused by the large interfacial resistance of LIC@LCO-10 wt% and LIC@LCO-5wt% (Fig. S10). To determine the change in the interfacial resistance, in-situ EIS was performed on LIC@LCO-15 wt% electrodes during the initial charge/discharge process (Fig. S11). The first semi-circle at the high-frequency region represents the resistance of the LIC layer, which is close to 78Ω . The resistance of the LIC layer does not undergo obvious change, implying the excellent stability of LIC upon cycling. The small semi-circle at the middle frequency represents the interfacial resistance between LIC@LCO, which is only 6.8Ω [29]. It should be mentioned that the ultra-small interfacial resistance is significantly smaller than those of sulfide/oxide-based AIBSBs, which generally shows the interfacial resistance of hundreds or thousands of ohms [21,25,40], implying that LIC@LCO-15 wt% electrodes have the fastest interfacial Li^+ transport among all the AIBSBs reported so far [5,16,21,40]. The middle-frequency semi-circle keeps stable during the initial

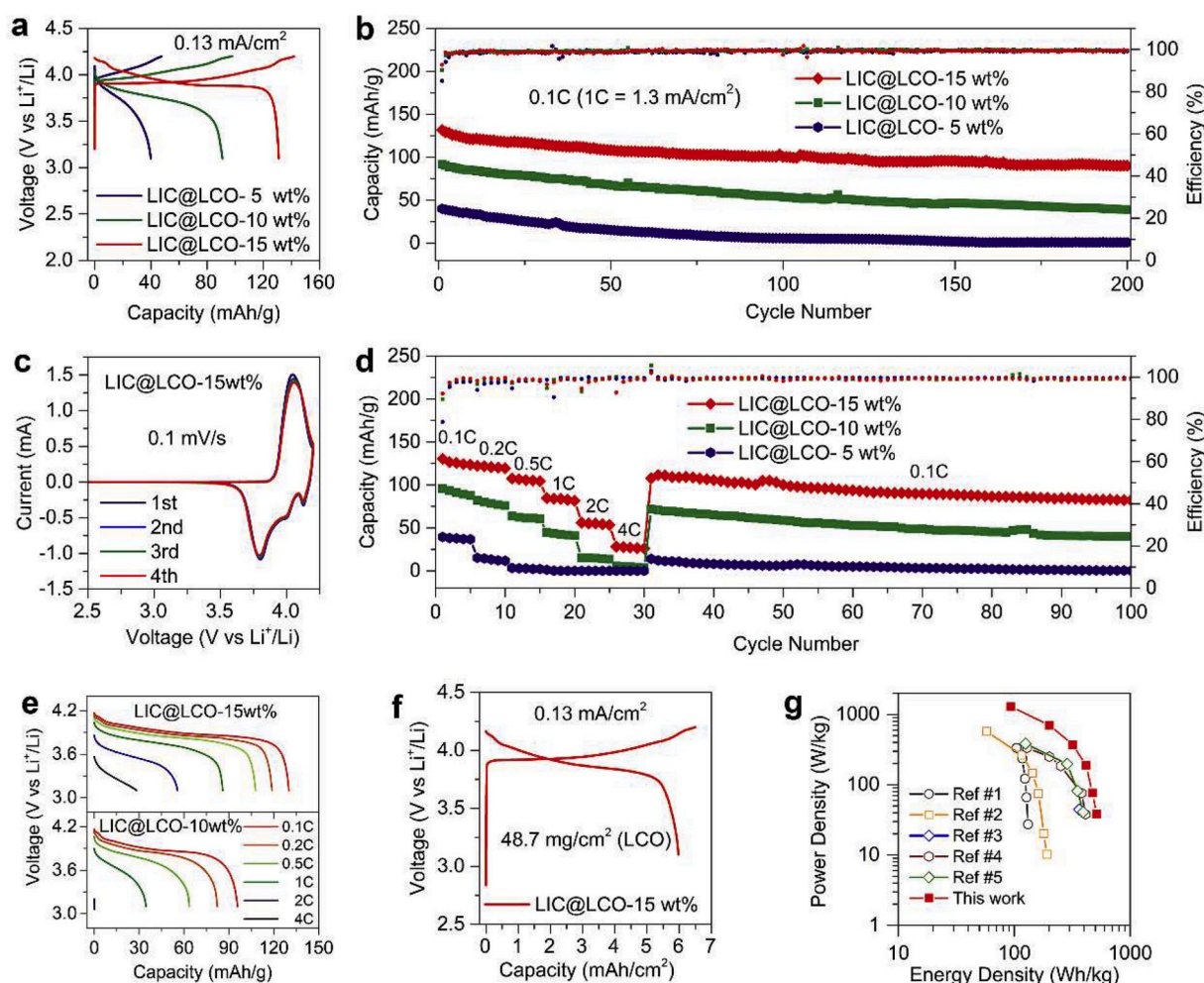


Fig. 3. Electrochemical performance of LIC@LCO electrodes. (a) initial charge/discharge curves of LIC@LCO electrodes with various ratios. (b) Cycling stability. (c) CV curves. (d) Rate Performance of LIC@LCO. (e) Discharge curves of LIC@LCO-15 wt% and LIC@LCO-10 wt% under various current densities. (f) Charge/discharge curves of high-loading LIC@LCO electrodes. (g) Ragone plot.

charge/discharge process, indicating that no interfacial reactions occurred between LIC and LCO upon cycling, which is due to the wide electrochemical window (up to 4.3V vs. Li^+/Li) of LIC [31,32].

Fig. 3b displays the cycling performance of LIC@LCO with different LIC contents. After 200 cycles, LIC@LCO with 15 wt% LIC keeps at 90.3 mAh g^{-1} with a CE of 99.3% while the LIC@LCO with 10 wt% LIC only remains at 39.1 mAh g^{-1} and LIC@LCO with 5 wt% LIC cannot be reversibly charged/discharged. Besides, LIC@LCO-15 wt% also demonstrated excellent cycling stability at 0.5C for 400 cycles (Fig. S12). The post-cycling analysis by SEM displays the well-maintained electrode structure after 100 cycles (Fig. S13), which also corroborates the excellent cycling stability of LIC@LCO-15 wt%. Fig. 3c shows the CV curves of LIC@LCO with 15 wt% LIC. The overlap of CV curves also indicates the stable cycling performance of LIC@LCO in AIBSBs. Fig. 3d displays the rate-performance of LIC@LCO with 15 wt% LIC. Even at 4C (5.2 mA cm^{-2}), LIC@LCO still shows a capacity of 28.5 mAh g^{-1} . Fig. 3e displays the corresponding discharge curves under different current densities. The corresponding power density of LIC@LCO-15 wt% is up to 1300 W kg^{-1} . Considering the high-loading electrode (13 mg cm^{-2}) in AIBSBs, the rate-performance of LIC@LCO is astonishing [41].

To determine the Li^+ kinetics of LIC@LCO-15 wt%, which is closely related to the power density of AIBSBs, the galvanostatic intermittent titration technique (GITT) was performed. The charge/discharge GITT curves, the small polarization curves, and the high Li^+ diffusion

coefficient ($\sim 10^{-9} \text{ cm}^2 \text{ s}^{-1}$) are presented in Fig. S14. The high Li^+ diffusion coefficient is even comparable with that in liquid cells [42]. That's why LIC@LCO-15 wt% demonstrates a high-rate performance up to 4C. The fast Li^+ kinetics of LIC@LCO-15 wt% is ascribed to the intimate solid-solid contact, high interfacial ionic conductivity, ultra-small interfacial resistance, as well as excellent interfacial stability. To meet the standards required for practical applications, a high areal capacity of LIC@LCO of 6 mAh cm^{-2} is also demonstrated with a high LCO loading of 48.7 mg cm^{-2} (Fig. 3f). Fig. 3g compares the power density and energy density of LIC@LCO-based AIBSBs with all previously reported results in the Ragone plot [4,17,21,25]. The sources of the data are listed in Table S5. Comparatively, LIC@LCO-15 wt% demonstrated the highest both energy density and power density of AIBSBs. Furthermore, the practical energy density of LIC@LCO composites was also fairly predicted as per practical pouch cell parameters [23]. As shown in Fig. S15, a high energy density over 300 Wh kg^{-1} ($>700 \text{ Wh L}^{-1}$) can be realized as long as a $50 \mu\text{m}$ ISE layer is provided.

In-situ/operando Raman spectroscopy was further performed to examine the interfacial stability between LIC and LCO upon cycling. The LIC@LCO electrode can be successfully charged to 118 mAh g^{-1} (Fig. 4a). LIC shows a broad peak at 191 cm^{-1} and a sharp and strong peak at 269 cm^{-1} , while LCO shows 478 cm^{-1} and 596 cm^{-1} , which are ascribed to E_g and A_{1g} vibrational modes of LCO, respectively [43]. These four peaks are detected and remain stable until 4.0V (Fig. 4b). The intensity of LCO peaks begins to decrease after 4.0V (highlighted by a

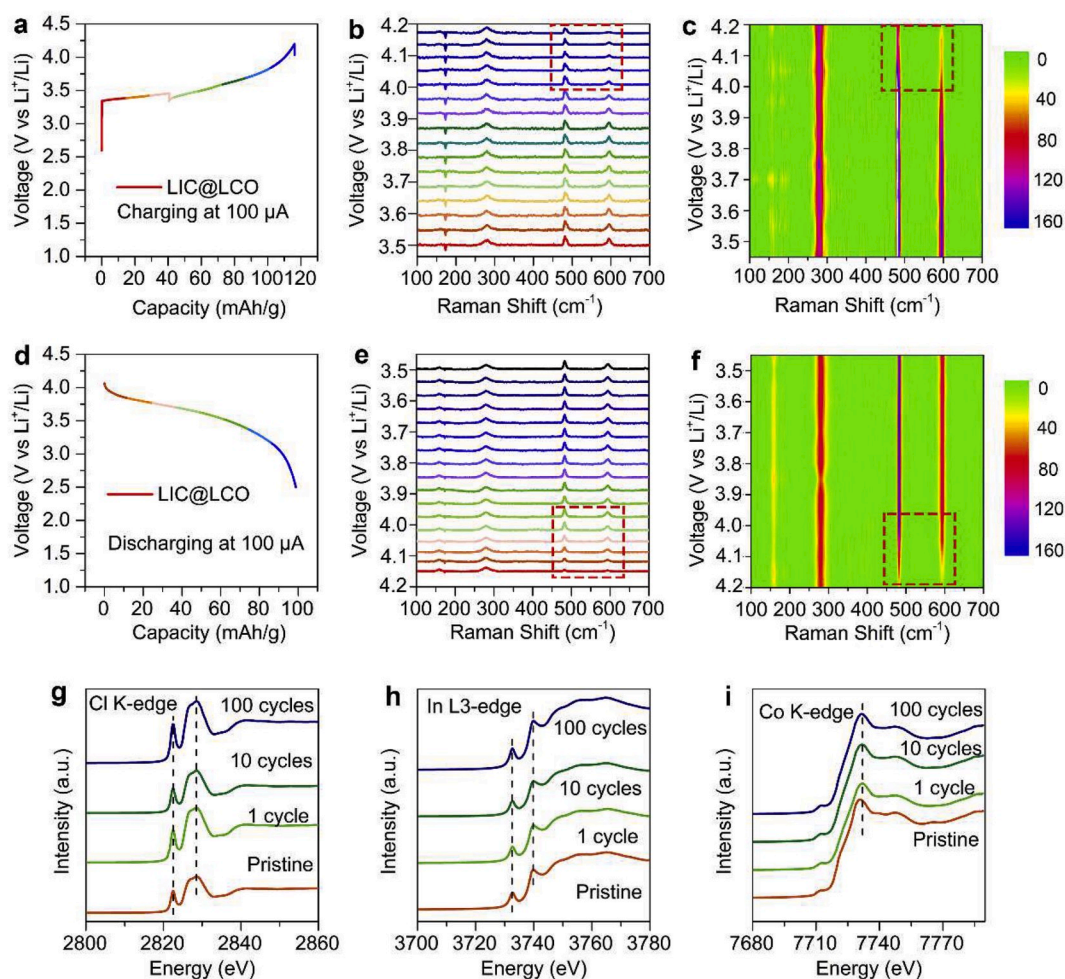


Fig. 4. In situ/operando Raman and ex-situ XAS spectra of LIC@LCO-15 wt% in AIBSBs. (a) Charging curves of LIC@LCO electrodes at the current density of 0.13 mA cm^{-2} . (b) Raman spectra of the LIC@LCO electrode during the charging process. (c) Contour plot of LIC@LCO during the charging process. (d) Discharging curves of LIC@LCO electrodes at the current density of 0.13 mA cm^{-2} . (e) Raman spectra of LIC@LCO electrodes during the discharging process. (f) Contour plot of LIC@LCO during the discharging process. (g) XANES of Cl K-edge. (h) XANES of In L3-edge. (i) XANES of Co K-edge.

red dash line), while LIC peaks remain the same, suggesting that the LIC is stable even at the high cut-off voltage (Fig. 4b). The contour plot of LIC@LCO during the charging process in Fig. 4c clearly shows the intensity decrease of peaks at 478 cm^{-1} and 596 cm^{-1} after charging to 4.0V, which is closely related to the de-lithiation of LCO upon charging and LCO lattice expansion [43]. No new peaks are detected during the charging process, suggesting that there are no side reactions between LIC and LCO upon charging. Fig. 4d shows the discharge capacity of 100 mAh g^{-1} . Fig. 4e shows the Raman spectra of LIC@LCO during the discharge process, the reduced peaks at 478 cm^{-1} and 596 cm^{-1} gradually recover from 4.2V to 4.0V and remain the same afterward, suggesting Li^+ is reversibly intercalated into the LCO layered structure. During the whole discharge process, LIC peaks remain the same, implying LIC is stable against LCO during the electrochemical cycling process.

Furthermore, ex-situ X-ray absorption spectroscopy was performed to investigate the interfacial stability between LIC and LCO after different cycles. Fig. 4g and h displays the Cl K-edge and In L3-edge of LIC@LCO-15 wt%, respectively. Compared to the pristine Cl K-edge and In L3-edge, the Cl K-edge and In L3-edge of LIC@LCO-15 wt% do not change even after 100 cycles, suggesting excellent interfacial stability during the electrochemical cycling. Fig. 4i shows the XAS spectra of Co K-edge, which also remains the same after the first cycle, implying the excellent electrochemical stability. The slight difference between the pristine Co K-edge and that after 1 cycle is ascribed to irreversible capacity loss during the first cycle. The in-situ Raman and ex-situ XAS analyses consistently confirm the excellent interfacial compatibility between LCO and LIC.

To further explore the interfacial stability between LCO and LIC, we calculated the binding energies of LCO(110)/LIC(100) and simulated their interfacial structure change under external electric fields of $\pm 0.3\text{ V/\AA}$, $\pm 0.2\text{ V/\AA}$, and $\pm 0.1\text{ V/\AA}$. As shown in Fig. 5b, the binding energy of the LCO(110)/LIC(100) interface generally increases with the electric field intensity, suggesting that the strength of interactions at the interface decrease under external electric fields. Especially, the LCO(110)/LIC(100) interface becomes more disordered for high electric field intensity and even breaks down under a potential of 0.3 V/\AA . Furthermore, we explored the variation of the Fermi level of interface structure, and it shows a similar trend as the binding energy (Fig. S16a). Besides, we also found that the LCO(110)/LIC(100) interface under 0.3 V/\AA shows an obvious bandgap (Fig. S16c), as compared with that for interface

structure under -0.3 V/\AA (Fig. S16b), indicating that the LCO/LIC interface structure is unstable under extremely high electric field intensity. In general, the actual electric field intensity that the battery undergoes is significantly smaller than $\pm 0.1\text{ V/\AA}$, in which the interfacial binding between LCO and LIC is very strong, which means the strong interfacial interaction can be well-maintained upon battery operation. The strong interfacial interaction also explains the ultra-stable long-cycling performance as shown in Fig. 3. The simulation results advance the understanding of the stability of the LCO/LIC interface and the structural evolution under external voltage.

3. Discussion

Here, we reported an in-situ interfacial growth of halide electrolytes (Li_3InCl_6 , LIC) on electrode materials (LiCoO_2 , LCO) directly from aqueous solution, which simultaneously improves the interfacial ionic conductivity and solid-solid ionic contact. To the best of our knowledge, this is the first time to demonstrate an interfacial-assisted in-situ synthesis of solid-state halide electrolytes on electrode materials with an ultrahigh ionic conductivity (1.5 mS cm^{-1}). There are several outstanding advantages of the in-situ interfacial growth of Li_3InCl_6 on electrodes for AIBSBs. Firstly, in-situ interfacial growth of LIC on LCO can form intimate solid-solid contact due to strong interfacial binding, thus constructing 3D Li^+ -transport pathways in LIC@LCO cathode composites. Secondly, no extra interfacial modification on LCO is required due to excellent interfacial stability between LCO and LIC. Due to the high ionic conductivity of LIC (1.5 mS cm^{-1}), the ultra-fast interfacial Li^+ -transport kinetics can be guaranteed. The average Li^+ diffusion coefficient is up to $10^{-9}\text{ cm}^2\text{ s}^{-1}$, which is even comparable to that of liquid cells. Therefore, LIC@LCO electrodes exhibited a high rate performance of 4C. The corresponding powder density is 1300 W kg^{-1} , which overtakes previous results. Thirdly, LIC@LCO-15 wt% demonstrates an ultra-small interfacial resistance of $6.8\text{ }\Omega$. The interfacial resistance is several orders of magnitude lower than those of mainstream sulfide/oxide-based AIBSBs [16]. Last but not least, as less as 15 wt% LIC is dispersed into cathode composites, which is significantly less than those in previous references (30% ISEs) [4,8,22]. Thus the high energy density (513 Wh.kg^{-1}) of AIBSBs is achieved in our case. We believed this method could be easily developed in pouch cells by in-situ solidification.

In summary, we successfully eliminated the interfacial resistance of

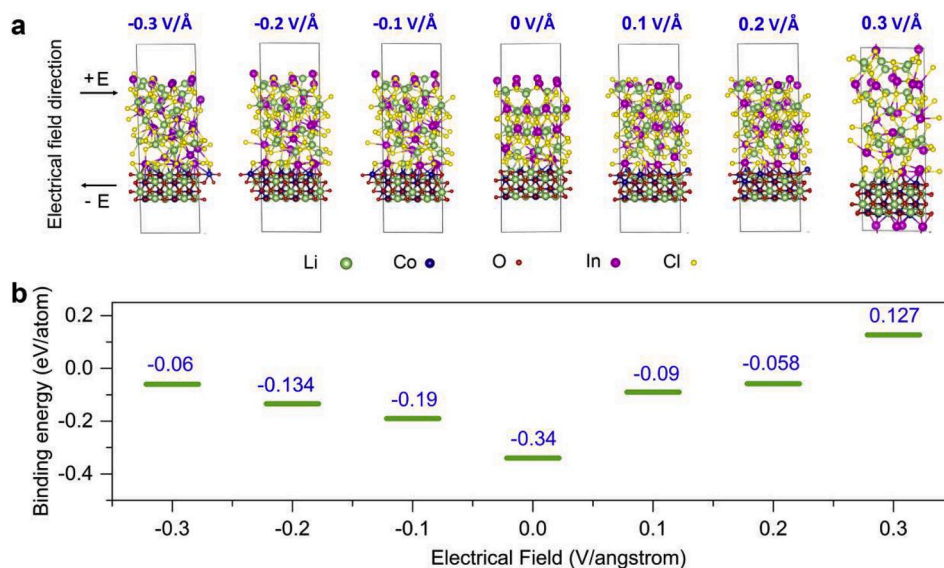


Fig. 5. (a) Illustration of a schematic view of LCO(110)/LIC(100) interface under the electrical field of -0.3 V/\AA , -0.2 V/\AA , -0.1 V/\AA , 0 V/\AA , 0.1 V/\AA , 0.2 V/\AA , and 0.3 V/\AA . (b) The variation of binding energy of LCO(110)/LIC(100) interface as a function of electric field strength.

AISBs by the in-situ interfacial growth of LIC. A strong interfacial interaction between LCO and LIC was found by XPS and DFT calculations, which is beneficial for the in-situ interfacial growth of LIC and the long-term cycling stability of AISBs. Benefiting from the high ionic conductivity (1.5 mS cm^{-1}) of LIC, intimate solid-solid contact, and high-voltage stability, the ultra-small interfacial resistance, LIC@LCO-15 wt% exhibited a high initial discharge capacity of 131.7 mAh.g^{-1} with an initial Coulombic efficiency of 92.7% at 0.1C. After 200 cycles, a capacity of 90.3 mAh.g^{-1} can be retained. Furthermore, the high-rate performance (28.5 mAh.g^{-1} at 4C) was achieved. Moreover, a high areal capacity of LIC@LCO up to 6 mAh.cm^{-2} was demonstrated with a high mass loading of 48.7 mg cm^{-2} (LCO). This facile approach offers a new route to overcome longstanding interfacial challenges in AISBs, enabling high-energy-density and high-power-density AISBs at room temperature.

Author contributions

C. W. and J. L. equally contributed to this work and designed all the experiments and characterizations. M. J. and S. M. performed theoretical calculations. X. L. helped with halide electrolyte synthesis. K. A. and M. B. helped with synchrotron characterizations. R. L. helped with purchasing all the chemicals. C. W. wrote the manuscript. All the authors discussed the results and commented on the manuscript. C. S. supervised the theoretical calculations. The whole project was supervised by X. S.

Declaration of competing interest

The authors declare that they have no known competing financial interests or personal relationships that could have appeared to influence the work reported in this paper.

CRediT authorship contribution statement

Changhong Wang: Conceptualization, Investigation, Writing - original draft. **Jianwen Liang:** Conceptualization, Investigation. **Ming Jiang:** Investigation, Formal analysis. **Xiaona Li:** Formal analysis. **Sankha Mukherjee:** Formal analysis. **Keegan Adair:** Writing - review & editing. **Matthew Zheng:** Formal analysis. **Yang Zhao:** Formal analysis. **Feipeng Zhao:** Formal analysis. **Shuming Zhang:** Writing - review & editing. **Ruying Li:** Resources. **Huan Huang:** Formal analysis. **Shang-qian Zhao:** Funding acquisition. **Li Zhang:** Funding acquisition. **Shi-gang Lu:** Funding acquisition. **Chandra Veer Singh:** Supervision. **Xueliang Sun:** Supervision, Conceptualization.

Acknowledgements

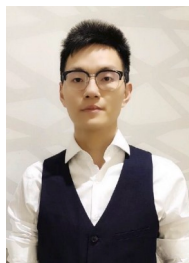
This work was supported by Natural Sciences and Engineering Research Council of Canada (NSERC), Canada Research Chair Program (CRC), Canada Foundation for Innovation (CFI), Ontario Research Fund, China Automotive Battery Research Institute Co., Ltd, GLABAT Solid-State Battery Inc., the Canada Light Source at University of Saskatchewan (CLS) and University of Western Ontario. J.L. and X. L. thank the support of Mitacs Elevate Postdoctoral Fellowship. C.W. appreciates the funding support of the Mitacs Accelerate Fellowship.

Appendix A. Supplementary data

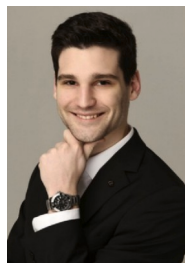
Supplementary data to this article can be found online at <https://doi.org/10.1016/j.nanoen.2020.105015>.

References

- [1] A. Manthiram, X. Yu, S. Wang, *Nat. Rev. Mater.* 2 (2017) 16103.
- [2] Y. Zhao, K. Zheng, X. Sun, *Joule* 2 (2018) 2583–2604.
- [3] J. Yue, F. Han, X. Fan, X. Zhu, Z. Ma, J. Yang, C. Wang, *ACS Nano* 11 (2017) 4885–4891.
- [4] N. Kamaya, K. Homma, Y. Yamakawa, M. Hirayama, R. Kanno, M. Yonemura, T. Kamiyama, Y. Kato, S. Hama, K. Kawamoto, A. Mitsui, *Nat. Mater.* 10 (2011) 682–686.
- [5] C. Wang, X. Li, Y. Zhao, M.N. Banis, J. Liang, X. Li, Y. Sun, K.R. Adair, Q. Sun, Y. Liu, *Small Methods* 3 (2019) 1900261.
- [6] J.-Y. Liang, X.-D. Zhang, X.-X. Zeng, M. Yan, Y.-X. Yin, S. Xin, W.-P. Wang, X.-W. Wu, J.-L. Shi, L.-J. Wan, Y.-G. Guo, *Angew. Chem. Int. Ed.* 59 (2020) 6585–6589.
- [7] F. Han, A.S. Westover, J. Yue, X. Fan, F. Wang, M. Chi, D.N. Leonard, N.J. Dudney, H. Wang, C. Wang, *Nat. Energy* 4 (2019) 187–196.
- [8] Y. Kato, S. Hori, T. Saito, K. Suzuki, M. Hirayama, A. Mitsui, M. Yonemura, H. Iba, R. Kanno, *Nat. Energy* 1 (2016) 16030.
- [9] K. Xu, *Chem. Rev.* 104 (2004) 4303–4418.
- [10] C. Wang, Y. Zhao, Q. Sun, X. Li, Y. Liu, J. Liang, X. Li, X. Lin, R. Li, K.R. Adair, L. Zhang, R. Yang, S. Lu, X. Sun, *Nano Energy* 53 (2018) 168–174.
- [11] F. Zhao, Q. Sun, C. Yu, S. Zhang, K. Adair, S. Wang, Y. Liu, Y. Zhao, J. Liang, C. Wang, X. Li, X. Li, W. Xia, R. Li, H. Huang, L. Zhang, S. Zhao, S. Lu, X. Sun, *ACS Energy Lett.* (2020) 1035–1043.
- [12] F. Han, J. Yue, X. Zhu, C. Wang, *Adv. Energy Mater.* 8 (2018) 1703644.
- [13] H. Duan, J. Zhang, X. Chen, X.-D. Zhang, J.-Y. Li, L.-B. Huang, X. Zhang, J.-L. Shi, Y.-X. Yin, Q. Zhang, Y.-G. Guo, L. Jiang, L.-J. Wan, *J. Am. Chem. Soc.* 140 (2018) 18051–18057.
- [14] J.-Y. Liang, X.-X. Zeng, X.-D. Zhang, T.-T. Zuo, M. Yan, Y.-X. Yin, J.-L. Shi, X.-W. Wu, Y.-G. Guo, L.-J. Wan, *J. Am. Chem. Soc.* 141 (2019) 9165–9169.
- [15] C. Wang, K.R. Adair, J. Liang, X. Li, Y. Sun, X. Li, J. Wang, Q. Sun, F. Zhao, X. Lin, R. Li, H. Huang, L. Zhang, R. Yang, S. Lu, X. Sun, *Adv. Funct. Mater.* (2019) 1900392, <https://doi.org/10.1002/adfm.201900392>.
- [16] Q. Zhang, D. Cao, Y. Ma, A. Natan, P. Aurora, H. Zhu, *Adv. Mater.* 31 (2019) 1901131.
- [17] N. Ohta, K. Takada, L. Zhang, R. Ma, M. Osada, T. Sasaki, *Adv. Mater.* 18 (2006) 2226–2229.
- [18] K. Takada, N. Ohta, L.Q. Zhang, X.X. Xu, B.T. Hang, T. Ohnishi, M. Osada, T. Sasaki, *Solid State Ionics* 225 (2012) 594–597.
- [19] Y. Xiao, L.J. Miar, Y. Wang, G. Ceder, *Joule* 3 (2019) 1252–1275.
- [20] C. Wang, J. Liang, S. Hwang, X. Li, Y. Zhao, K. Adair, C. Zhao, X. Li, S. Deng, X. Lin, X. Yang, R. Li, H. Huang, L. Zhang, S. Lu, D. Su, X. Sun, *Nano Energy* 72 (2020) 104686.
- [21] W. Zhang, D.A. Weber, H. Weigand, T. Arlt, I. Manke, D. Schröder, R. Koerver, T. Leichtweiss, P. Hartmann, W.G. Zeier, J. Janek, *ACS Appl. Mater. Interfaces* 9 (2017) 17835–17845.
- [22] B. Wu, S. Wang, W.J. Evans Iv, D.Z. Deng, J. Yang, J. Xiao, *J. Mater. Chem.* 4 (2016) 15266–15280.
- [23] L. Liu, J. Xu, S. Wang, F. Wu, H. Li, L. Chen, *eTransportation* 1 (2019) 100010.
- [24] D.H. Kim, D.Y. Oh, K.H. Park, Y.E. Choi, Y.J. Nam, H.A. Lee, S.-M. Lee, Y.S. Jung, *Nano Lett.* 17 (2017) 3013–3020.
- [25] K.H. Park, D.Y. Oh, Y.E. Choi, Y.J. Nam, L. Han, J.-Y. Kim, H. Xin, F. Lin, S.M. Oh, Y.S. Jung, *Adv. Mater.* 28 (2016) 1874–1883.
- [26] A. Miura, N.C. Rosero-Navarro, A. Sakuda, K. Tadanaga, N.H.H. Phuc, A. Matsuda, N. Machida, A. Hayashi, M. Tatsumisago, *Nat. Rev. Chem.* 3 (2019) 189–198.
- [27] L. Zhou, K.-H. Park, X. Sun, F. Lalère, T. Adermann, P. Hartmann, L.F. Nazar, *ACS Energy Lett.* 4 (2018) 265–270.
- [28] S. Mui, J. Voss, R. Schlem, R. Koerver, S.J. Sedlmaier, F. Maglia, P. Lamp, W. G. Zeier, Y. Shao-Horn, *iScience* 16 (2019) 270–282.
- [29] T. Asano, A. Sakai, S. Ouchi, M. Sakaida, A. Miyazaki, S. Hasegawa, *Adv. Mater.* 30 (2018) 1803075.
- [30] X. Li, J. Liang, J. Luo, M.N. Banis, C. Wang, W. Li, S. Deng, C. Yu, F. Zhao, Y. Hu, *Energy Environ. Sci.* 12 (2019) 2665–2671.
- [31] S. Wang, Q. Bai, A.M. Nolan, Y. Liu, S. Gong, Q. Sun, Y. Mo, *Angew. Chem. Int. Ed.* 58 (2019) 8039–8043.
- [32] X. Li, J. Liang, X. Yang, K.R. Adair, C. Wang, F. Zhao, X. Sun, *Energy Environ. Sci.* (2020), <https://doi.org/10.1039/C1039EE03828K>.
- [33] J. Liang, X. Li, S. Wang, K.R. Adair, W. Li, Y. Zhao, C. Wang, Y. Hu, L. Zhang, S. Zhao, *J. Am. Chem. Soc.* 142 (2020) 7012–7022.
- [34] M.-C. Nguyen, M. Jang, D.-H. Lee, H.-J. Bang, M. Lee, J.K. Jeong, H. Yang, R. Choi, *Sci. Rep.* 6 (2016) 25079.
- [35] J. Qian, L. Liu, J. Yang, S. Li, X. Wang, H.L. Zhuang, Y. Lu, *Nat. Commun.* 9 (2018) 1–11.
- [36] K.H. Park, Q. Bai, D.H. Kim, D.Y. Oh, Y. Zhu, Y. Mo, Y.S. Jung, *Adv. Energy Mater.* 8 (2018) 1800035.
- [37] L. Dahéron, H. Martinez, R. Dedryvere, I. Baraille, M. Ménétrier, C. Denage, C. Delmas, D. Gonbeau, *J. Phys. Chem. C* 113 (2009) 5843–5852.
- [38] Y. Shao-Horn, L. Croguennec, C. Delmas, E.C. Nelson, M.A. O’Keefe, *Nat. Mater.* 2 (2003) 464–467.
- [39] J. Haruyama, K. Sodeyama, Y. Tateyama, *ACS Appl. Mater. Interfaces* 9 (2017) 286–292.
- [40] W.J. Li, M. Hirayama, K. Suzuki, R. Kanno, *Solid State Ionics* 285 (2016) 136–142.
- [41] Y. Kuang, C. Chen, D. Kirsch, L. Hu, *Adv. Energy Mater.* 9 (2019) 1901457.
- [42] Q. Liu, X. Su, D. Lei, Y. Qin, J. Wen, F. Guo, Y.A. Wu, Y. Rong, R. Kou, X. Xiao, *Nat. Energy* 3 (2018) 936–943.
- [43] E. Flores, P. Novák, E.J. Berg, *Front. Energy Res.* 6 (2018), <https://doi.org/10.3389/fenrg.2018.00082>.



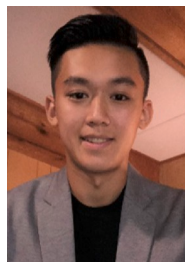
Dr. Changhong Wang is currently a research scientist in GLA-BAT Solid-State Inc. Canada. He obtained his M.S. degree in materials engineering in 2014 from University of Science and Technology of China (USTC) and received his Ph.D. degree in Mechanical and Materials Engineering from the University of Western Ontario (UWO), Canada. He also served as a research assistant in Singapore University of Technology and Design (SUTD) from 2014 to 2016. Currently, his research interests include solid-state sulfide electrolytes, all-solid-state batteries, and bio-inspired artificial synapses.



Keegan Adair received his B.Sc. in chemistry from the University of British Columbia in 2016. He is currently a Ph.D. candidate in Prof. Xueliang (Andy) Sun's Nanomaterials and Energy Group at the University of Western Ontario, Canada. Keegan has previously worked on battery technology at companies such as E-One Moli Energy and General Motors. His research interests include the design of nanomaterials for lithium metal batteries and nanoscale interfacial coatings for battery applications.



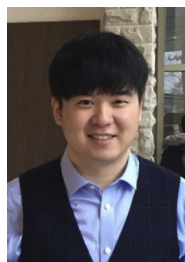
Dr. Jianwen Liang received his Ph.D. degree in inorganic chemistry from University of Science and Technology of China in 2015. He is currently a postdoctoral fellow in Prof. Xueliang (Andy) Sun's Nanomaterials and Energy Group at the University of Western Ontario, Canada. His research interests include sulfide-based solid-state electrolyte as well as all-solid-state Li/Li-ion batteries.



Matthew Zheng is currently an undergraduate engineering student at the University of British Columbia (UBC). He was a visiting student for the summer at the University of Western Ontario (UWO) in 2017 and 2018. His research focuses on the application of 3D printing techniques in LIB design with a particular focus on solid state LIBs.



Ming Jiang is currently a joint Ph.D. candidate in Prof. Chandra Veer Singh's group at the University of Toronto, Canada. He focuses on the first-principles and *ab initio* molecular dynamics simulation of the electronic, mechanical and transport properties of solid-state electrolytes.



Dr. Yang Zhao is currently postdoctoral fellow in Prof. Xueliang (Andy) Sun's Group at the University of Western Ontario, Canada. He received his B.S. degree and M.S. degree in Chemical Engineering and Technology from Northwestern Polytechnical University (Xi'an, China) in 2011 and 2014, respectively. His current research interests focus on atomic/molecular layer deposition in the application of lithium/sodium ion batteries and all solid state batteries.



Dr. Xiaona Li is a postdoctoral associate in Prof. Xueliang (Andy) Sun's Group at the University of Western Ontario (Western University), Canada. She received her B.S. degree in Material Chemistry in 2011 from Sichuan University and Ph.D. degree in Inorganic Chemistry in 2015 under the supervision of Prof. Dr. Yitai Qian on the study of electrode materials synthesis for Li^+/Na^+ batteries from University of Science and Technology of China. She joined Prof. Sun's group in 2017 and her current research interests focus on the synthesis of sulfide solid electrolytes and all-solid-state batteries.



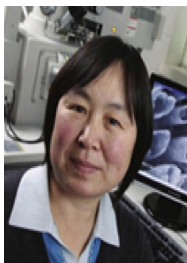
Feipeng Zhao is currently a Ph.D. candidate in Prof. Xueliang (Andy) Sun's Group at the University of Western Ontario, Canada. He received his B.S. degree and M.S. degree in Materials Science from Soochow University in 2017 and 2014, respectively. Currently, he is working on the synthesis and characterization of sulfide electrolytes, and development of high-performance solid-state Li metal and Na metal batteries.



Dr. Sankha Mukherjee is a theorist who studies behavior of materials across length scales through atomistic computational techniques. He is interested in using these techniques to study, (a) mechanical properties of materials from the small scale of atomically thin systems up to as large as nanosheets and understand (b) chemical interactions at the interphases of Li-based batteries to materials for applications as electrodes. Sankha received his undergraduate education in Metallurgical Engineering from Bengal Engineering and Science University, Shibpur. After a brief stint in industry, he resumed his academic journey at IIT Bombay as a master's student in the Materials Science program. Thereafter, he earned a PhD in the Mechanical Engineering department at McGill University. Currently, Sankha is a postdoctoral fellow in the department of Materials Science and Engineering at the University of Toronto.



Shumin Zhang is currently a Ph.D. candidate in Prof. Xueliang (Andy) Sun's group at the University of Western Ontario, Canada. She received her B.S. degree in Textile Engineering (2016) and M.S. degree in Material Science and Engineering (2019) from Soochow University. Currently, her research interests focus on synthesis and characterization of sulfide electrolytes and halide electrolytes in all-solid-state batteries.



Ruying Li is a research engineer at Prof. Xueliang (Andy) Sun's Nanomaterial and Energy Group at the University of Western Ontario, Canada. She received her master in Material Chemistry under the direction of Prof. George Thompson in 1999 at University of Manchester, UK, followed by work as a research assistant under the direction of Prof. Keith Mitchell at the University of British Columbia and under the direction of Prof. Jean-Pol Dodelet at l'Institut national de la recherche Scientifique (INRS), Canada. Her current research interests are associated with synthesis and characterization of nanomaterials for electrochemical energy storage and conversion.



Dr. Shigang Lu is Vice president of China Automotive Battery Research Institute Co., Ltd. He has the responsibility for technology innovations in the area of automotive battery application. He has extensive experience in many energy research areas including fuel cells, and lithium-ion batteries. Dr. Lu received her Ph.D. degree in Chemistry from Moscow State University in 1993. He has extensive experience in novel material processing techniques for automotive battery applications. His current research interests include new energy electrochemistry, lithium-ion battery and related materials, solid-state battery and related materials.



Dr. Huan (Henry) Huang received his Ph.D. from University of Waterloo in 2002. He is currently a General Manager for the company. He has extensive experience in lithium ion cylindrical cells and served as a Research Scientist at E-One Moli Energy Corp., before managing GLABAT. His research interests focus on the development and commercialization of solid-state batteries with robust and consistent performance.



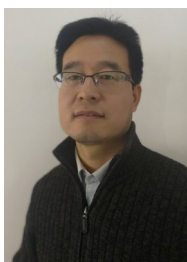
Prof. Chandra Veer Singh is the Erwin Edward Hart Endowed Associate Professor and Associate Chair of Research in the Department of Materials Science and Engineering (MSE) at the University of Toronto, Canada. Dr. Singh received his Ph.D. in Aerospace Engineering in 2008 from Texas A&M University. Subsequently, he worked as a postdoctoral fellow at Cornell University. He obtained industrial experience as a Design Engineer at General Electric Aircraft Engines. His research is currently focused on the atomistic modeling and machine learning enabled development of new materials for applications in electrochemical energy conversion and storage, including catalysts and metal-ion batteries.



Dr. Shangqian Zhao received his B.S. degree in Physics from Jilin University in 2009 and his Ph.D. degree in Condensed Matter Physics from Institute of Physics, Chinese Academy of Sciences in 2014. He is currently a senior scientist of China Automotive Battery Research Institute Co., Ltd., Beijing, China. His research interests focus on mass production of solid electrolytes and development of high-capacity solid-state Li/Li-ion batteries.



Prof. Xueliang (Andy) Sun is a Canada Research Chair in Development of Nanomaterials for Clean Energy, Fellow of the Royal Society of Canada and Canadian Academy of Engineering and Full Professor at the University of Western Ontario, Canada. Dr. Sun received his Ph.D. in materials chemistry in 1999 from the University of Manchester, UK, which he followed up by working as a postdoctoral fellow at the University of British Columbia, Canada and as a Research Associate at L'Institut National de la Recherche Scientifique (INRS), Canada. His current research interests are focused on advanced materials for electrochemical energy storage and conversion, including electrocatalysis in fuel cells, solid-state batteries, and metal-air batteries.



Dr. Li Zhang is currently a senior scientist of China Automotive Battery Research Institute Co., Ltd., Beijing, China. He received his Ph.D. degree in Electrochemistry from University of Science & Technology Beijing, China in 2009. He has more than 10 years of power sources experience with expertise in battery materials as well as electrode design. Currently, his research interests include solid-state electrolytes, all-solid-state Li-air, and lithium batteries.